Article

Effects of Static Stability Margin on Aerodynamic Design Optimization of Truss-Braced Wing Aircraft

Li Li [1], Lei Qiao [2,*], Jiakuan Xu [1] and Junqiang Bai [1,2]

[1] School of Aeronautics, Northwestern Polytechnical University, Xi'an 710072, China; lili_chris@mail.nwpu.edu.cn (L.L.); k.xu@nwpu.edu.cn (J.X.); junqiang@nwpu.edu.cn (J.B.)

[2] Unmanned System Research Institute, Northwestern Polytechnical University, Xi'an 710072, China

* Correspondence: ql@nwpu.edu.cn

Abstract: Currently, the aviation industry is facing an oil and energy crisis and is contributing much more greenhouse gas emissions to the environment. Aircraft design approaches, such as aerodynamic shape optimization, new configuration concepts, and active control technology, have been the primary and effective means of achieving goals concerning fuel burn, noise, and emissions. For now, the design problems of relaxed static stability (RSS, an active control technique) and truss-braced wing (TBW) configurations with high-fidelity aerodynamic shape optimization methods have been investigated widely to promote aerodynamic performance. Nevertheless, they are studied almost always separately, and the combination of exploration and refined design is rarely presented. Therefore, the purposes of this work are to evaluate the benefits of RSS on a full TBW wing–body–tail configuration under various flight conditions and the effects on multi-components and to further explore the potential and analyze the aerodynamic features with the combination of shape optimization and RSS. To address these issues, on the one hand, a range of seven static stability margins are adopted to evaluate its effects with a high-fidelity Reynolds-averaged Navier–Stokes solver. On the other hand, seven cases of drag minimization multipoint aerodynamic design optimization are performed, which are with 600 shape variables and 13 twist variables, subject to lift coefficient, trim, and thickness constraints. The results indicate that with RSS only, the initial configuration has a 2.39% drag reduction under cruise conditions and a 3.01% and a 5.24% drag reduction under two off-design conditions. Additionally, the effects on the multi-components are observed and analyzed. Moreover, all of the optimized configurations with RSS have 2.13%, 2.42%, and 2.12% drag reductions under cruise conditions, drag divergence conditions, and near-buffet-onset conditions, respectively. The most promising optimized configuration has a lift-to-drag ratio of 24.48 with an aerodynamic efficiency of 17.14. The evaluations with a series of off-design points also present high-level aerodynamic efficiency.

Keywords: truss-braced wing aircraft; aerodynamic design optimization; relaxed static stability; aerodynamic efficiency; drag reduction

1. Introduction

With the rapid development of economic globalization, the whole world is becoming a tightly connected life circle, and fast and efficient aviation flights have played a significant role in supporting this tendency. Meanwhile, there has been a dramatic increase in global routes, and a noticeable upward trend can be found in increased air travel. According to the market forecast data published via global commercial aircraft companies, including Airbus, Boeing, and the Commercial Aircraft Corporation of China (COMAC), it is estimated that by 2037, the commercial aviation market will reach a tremendous demand, with 8000 million passengers and 48,000 aircraft [1]. Nevertheless, this enormous consumption of aviation fuel has a growing adverse impact on the environment. On the basis of the research data released by the International Air Transport Association (IATA), the aviation industry produces approximately 2–3% of the total man-made carbon dioxide emissions. When

taking into account the nitrogen oxides by combustion, soot particles, and contrail cirrus due to cloud formation, it contributes approximately 5% to all greenhouse gas emissions. Moreover, oil prices are still high in the current economic situation, and more than 20% of operating costs are spent on fuel consumption for a single flight. In addition, the world is facing an oil and energy crisis to a certain extent. All of these issues drive the entire aviation industry to explore innovative aircraft design methods to improve fuel efficiency, reduce air pollution, and achieve green flight [2,3].

The National Aeronautics and Space Administration (NASA) proposed a strategic research plan for future ultra-green aircraft concepts ("N + 4") [4–7]. The long-term vision of this program is to improve the performance of the aircraft entering service in 2025–2035 and to study a series of new aircraft types and the corresponding vital technological evolution. The Subsonic Ultra Green Aircraft Research (SUGAR) team led by Boeing developed a worldwide comprehensive development vision for future commercial aviation. They selected a range of conventional configurations, unconventional configurations, and some potentially innovative technologies, which are applied to analyze their ability to reduce noise and emissions, assess the corresponding technical risks, and design a technology roadmap7. A three-step strategy was announced for the aviation industry by IATA to cut greenhouse gas emissions [8,9]. The International Civil Aviation Organization (ICAO) proposed more stringent regulations for future aircraft noise, CO_2 emissions, and NOx emissions [10,11]. Furthermore, there are the Clean Sky program and "Flightpath 2050" in Europe [12,13]. Based on the developments and achievements of these projects, there is an important conclusion that reducing the fuel consumption of aircraft is closely related to improving flight performance. Even if aerodynamic efficiency is improved slightly, it can obtain a non-negligible benefit in noise and emissions reduction. As a result, design methods such as aerodynamic design optimization, the exploration of new aircraft concepts, and active control technology have been the primary and effective means to provide better aerodynamic performance.

In the exploration of new aircraft layouts, blended wing body (BWB)/hybrid wing body (HWB), double-bubble (D8), and strut-braced wing (SBW)/truss-braced wing (TBW), as novel configurations, have the ability and large potential to reduce drag and/or weight, which has attracted much attention from research institutions and university work teams around the world [14,15]. Among them, TBW aircraft, with large spans and high aspect ratio wings, as well as a lower sweep and thinner thickness, are one of the most promising innovative designs for the next-generation airliner from both economic and environmental perspectives [16].

As for the high-fidelity aerodynamic optimization design method, it can rapidly and effectively explore the design space within the variable range for a given design objective while satisfying the design constraints. There is no difference between traditional aircraft and unconventional ones, as the method is able to provide a refined robust design with further detailed analyses, and it also helps understand the aerodynamic potential and tradeoffs better. Considering the shape complexity of a full TBW wing–body–tail configuration, it is indispensable that it is designed with high-fidelity and large-scale refined aerodynamic shape optimization [17].

Speaking of active control technology, it has been widely applied in the aircraft design field during the past few decades. Relaxed Static Stability (RSS), as one of the effective active control approaches, relaxes the requirements for the static stability margin, making it deliberately less than conventional design values, and it is already utilized in most of the new designs of fly-by-wire airliners. The stability margin of an aircraft is highly interrelated with aerodynamic efficiency, and so RSS is extremely beneficial for improving the performance of the aircraft: reducing the drag, lowering the structural weight, and increasing the useful lift, as well as enhancing the overload capacity, increasing the turning velocity, and shortening the turning radius. Meanwhile, it should be noted that aircraft with RSS technology require an active control system to exhibit nominal flying qualities, which may deteriorate to alternate or direct modes in the case of serious failures.

For now, in the design problems with SBW/TBW configurations, the design methods range from the multidisciplinary design optimization (MDO) approach to a single-discipline perspective. For the application of the MDO system, the works of [18–20] clearly presented its potential benefits, which include the reduction in noise and fuel consumption, along with excellent overall flight performance. Additionally, it could help designers trade the technology synthesis better by understanding the entire design space, particularly during the conceptual design phase. For the structural design, papers [21,22] investigated the wing's structural and aeroelastic performance, investigating the influence of wing parameters on the flutter speed, wing weight, and natural frequencies. A flutter analysis method was developed to analyze the variations of the amplitude and phase shift under unsteady transonic flow. For the propulsive system design, the researchers in [23,24] built their own propulsion modules to evaluate fuel burn and fuel efficiency. Chau and Zingg used statistical correlations to provide available thrust and TSFC for a specific speed and altitude. Lee et al. presented the effects of engine installation on engine fuel efficiency through an integrated design module. For the individual aerodynamic aspect, the studies conducted in [25–27] were concerned with airfoil design, fairing design, and cruise speed. They provided insights into aerodynamic performance, potential drag reduction, and the effect of natural laminar flow technology. In addition, there are some works [28,29] that address the design problems associated with the SBW/TBW configuration by employing the high-fidelity aerodynamic shape optimization method. They investigated the reduction in shocks and separation in the wing–strut junction region, redesigned the junction part with shape optimization, and explored the potential optimal shape.

As for the design problems involving the static stability margin, there are also a number of remarkable works that contribute to performance improvement. Firstly, this approach has been applied in research aimed at designing various aircraft configurations. The examples range from civil transport aircraft [30–32], conceptual BWB configurations [1,33,34] to other unconventional aircraft [35,36] and some unmanned airplanes [37,38]. Secondly, various achievements have been made in exploring the effects of this technique on the tradeoffs or benefits in terms of aircraft design [1,33,39]. For instance, the study in [1] presented that a higher L/D could be achieved by relaxing the static stability margin. The work in [33] discussed the relation between relaxed static stability, aerodynamic performance, and the direct operating cost (DOC) of civil aircraft. Moreover, some works connected static stability characteristics with improved aerodynamic efficiency in aerodynamic shape optimization issues, which led to the development of an effective and efficient method of studying optimal shape design under the balance between aerodynamic performance, static stability, and trim drag [34,40].

During the preliminary design phase of a TBW configuration, previous studies with an MDO system played a significant role in exploring performance and potential across different complicated disciplines and future promising innovative technologies. However, for computational savings, the MDO approach generally used low-fidelity solvers and low-order models, where some detailed performances and the effects of individual disciplines were sometimes not considered. Additionally, it can be found that all these optimization designs were meant to exploit the aerodynamic potentials of the SBW/TBW configuration, quantify the associated benefits, and address the complex flow issues associated with such configurations. Nevertheless, to fully investigate the aerodynamic potentials and explore the complicated interaction among the wing, fuselage, and struts specifically, it is significant to perform a refined comprehensive aerodynamic design that considers both the cruise and off-design conditions. Additionally, it is necessary to concentrate on the complete TBW wing–body–tail configuration to a certain extent. In addition, current aerodynamic studies focusing on the static stability margin have made significant contributions to the design potential and performance improvement of civil commercial airplanes, including traditional tube and wing configurations (narrow-body/wide-body aircraft) and conceptual BWB/HWB configurations. However, up to now, it has rarely been applied in the exploration and design of SBW/TBW geometry. In order to fully investigate and quantify

the aerodynamic benefits of this promising innovative configuration, it is essential to carry out high-fidelity aerodynamic studies, enabling an evaluation of the tradeoffs between aerodynamic efficiency, trim and static stability margin.

Driven by the cited papers, this work mainly has two purposes: (1) for a full TBW wing–body–tail configuration, to examine how much more aerodynamic efficiency can be improved only by the application of relaxed static stability under both on-design and off-design flight conditions, and to analyze its effect on the multi-components, such as the wing, tail, struts, and intersections; (2) in consideration of combining relaxed static stability with the aerodynamic shape optimization approach, to perform high-fidelity comprehensive aerodynamic designs to evaluate and analyze the associated effects, potentials, and tradeoffs.

For the former target, firstly, we shape the initial TBW geometry based on the Boeing SUGAR High-Revision D configuration. Subsequently, a high-fidelity RANS solver is employed with a generated multi-block structured grid to discuss the aerodynamic performance and detailed complex flow characteristics. The cruise condition is $M = 0.70$ and $C_L = 0.77$, which is unusual when compared to a traditional tube-and-wing single-aisle aircraft with nearby $M = 0.78$ and $C_L = 0.5$. The off-design conditions are chosen with the drag divergence condition and the near buffet-onset condition, which are crucial and indispensable aspects of civil transonic aircraft design. We adopt seven static stability margins to evaluate its effects. For the latter target, we perform seven cases of multipoint aerodynamic design optimization with 600 shape variables and 13 twist variables in a structured mesh, where each optimization case corresponds to a static stability margin.

The present work is organized as follows. Section 2 will describe the numerical tools briefly, including the CFD solver and geometric parameterization, as well as the mesh deformation algorithm and gradient-based optimization algorithm. After that, in Section 3, we will introduce the problem statement to illustrate the baseline geometry, the definition of static stability margin and the study cases considered in this paper. Section 4 will discuss the research results, followed by the conclusions at the end.

2. Methodology

In this section, the methods and numerical tools used in this work will be introduced briefly. Based on these modules, an aerodynamic shape optimization system with a high-fidelity solver and a gradient-based optimizer is built. This system has been widely applied by the author's group and other teams in the field of civil aircraft aerodynamic design [17,41–45]. The specific workflow of the design system is shown in Figure 1.
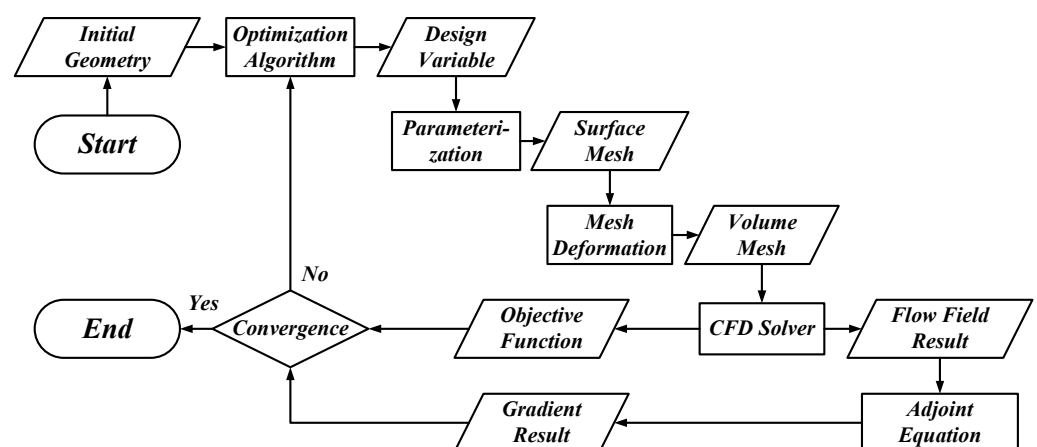
Figure 1. Workflow of the aerodynamic shape optimization system.

2.1. CFD Solver

In this paper, we use the ADflow developed by MDO Lab (as an open-source code) [46] as the CFD solver. It is able to solve both RANS and Euler equations. For our analysis,

we adopt three-dimensional RANS equations to evaluate the high-fidelity aerodynamic performance. For spatial discretization, a Jameson–Schmidt–Turkel (JST) scheme is applied. For the turbulence model, a Spalart–Allmaras (SA) one-equation turbulence equation is used. For the time-marching method, the diagonally dominant alternating direction implicit (D3ADI) method is adopted. Additionally, in order to improve the efficiency of calculation, an implicit residual smoothing and multigrid algorithm, as well as parallel computing and local time stepping, are used.

2.2. Geometric Parameterization

This paper adopts the B-spline-based Free-Form Deformation (FFD) method to parameterize the whole TBW geometry. The FFD approach has been applied widely in aerodynamic optimization designs [42–45,47–49]. For this method, it mainly has two advantages: firstly, it need not interpolate or fit the baseline configuration, and it only needs fewer design variables to manage the aerodynamic shape deformation. Secondly, it possessed a remarkable attribute of maintaining geometry continuity, enabling its application on both local and global scales, ensuring derivative continuity. Additionally, it allows for the imposition of local deformations with any desired degree of derivative continuity while maintaining geometric properties such as topological relationship and smoothness. An open-source code called pyGeo is utilized as the parameterization module, and a comprehensive explanation of that can be accessed in reference [50].

2.3. Mesh Deformation Algorithm

Due to the intricate geometry of the entire TBW wing–body–tail configuration, including the fairing parts and intersecting regions that connect the fuselage, wing, and struts, it becomes essential for the mesh deformation algorithm to effectively handle challenges such as maintaining robustness and significant mesh perturbations. Moreover, it should possess strong control capabilities for mesh torsion and displacement. As a result, we employ the inverse distance weighting (IDW) algorithm [51,52], known as an algebraic interpolation technique. The procedure involves converting the surface mesh perturbation, such as torsion and translation, into the spatial mesh using the IDW function. Subsequently, the spatial mesh is updated accordingly. The approach offers improved efficiency as it eliminates the need for solving linear or nonlinear equations in the algorithm. The utilized code module for this paper is idwarp, an open-source package developed by the MDO Lab [53].

2.4. Gradient-Based Optimization Algorithm

In this study, the sequential quadratic programming (SQP) optimization algorithm is employed as the gradient-based optimizer. The SQP algorithm, chosen for its high efficiency and ability to handle large-scale design variables and function constraints [54,55], is a prominent gradient optimizer widely employed in current practices and has found extensive application in various engineering problems [56–58]. The fundamental concept revolves around transforming constrained nonlinear optimization problems into subproblems of quadratic programming at each iteration. This involves solving the optimization problem of the corrected Lagrangian quadratic model, taking into account linearized constraints. The associated code module employed is pyOptSparse, an open-source package developed by the MDO Lab [59].

3. Problem Statement

3.1. Static Stability Margin

For an aircraft, stability is the tendency to return to a state of equilibrium after a perturbation, which includes static stability and dynamic stability. Static stability represents the response of instantaneous force and the moment when the aircraft is disturbed slightly and deviates from the originally steady state, and the aircraft can return to stable conditions after the disturbances disappear. To ensure the safety and manageability of an aircraft,

the stability characteristics are vitally significant. In this work, the definition of static longitudinal stability margin (K_n) is referred to the papers [60] with two expressions:

$$K_n = (x_n - x_{CG})/\text{MAC} \tag{1}$$

$$K_n = -C_{m\alpha}/C_{L\alpha} \tag{2}$$

where x_{CG} and x_n are the locations of the center of gravity and neutral point, respectively, MAC is the mean aerodynamic chord, and $C_{m\alpha}$ and $C_{L\alpha}$ are the derivatives of the pitch moment coefficient and lift coefficient with respect to the angle of attack. Thus, it is clear that the aircraft is statically stable when $K_n > 0$, and it is unstable when $K_n < 0$. The calculation of the static stability margin refers to Reist's study [34], which is a $\Delta\alpha = 0.1$ deg method via a finite difference with respect to the angle of attack.

Relaxed static stability can be achieved by either moving the center of gravity backward [32,61] or by shifting the aerodynamic center forward [31,62]. The more aft center of gravity leads to a smaller trim drag, which can be realized with a shorter fuselage length, like the design utilized in Boeing's transport aircraft, or an extra fuel tank at the rear airframe, like the design utilized in the Concorde supersonic aircraft. The more forward aerodynamic center is usually reached by a smaller horizontal tail to reduce structural weight and friction drag, such as in the B-52 CCV design, or by a canard layout employed in fighter aircraft [38].

3.2. Baseline Full Configuration Geometry

Based on the Boeing SUGAR High-Revision D model, this paper shapes the initial full TBW wing–body–tail configuration [63], which is shown in Figure 2. The detailed geometric parameters can be found in [17]. In this paper, we continue to utilize three positions along the wing to establish the initial airfoils: the wing root section, wing kink section, and wingtip section. The thickness-to-chord ratio (t/c) for these sections remains consistent with the previous work, with values of 12.74%, 9.68%, and 9.42%, respectively [17]. However, there are some differences in the selection of baseline airfoils. This time, we adopt these three baseline airfoils from the SBW configuration provided by the PADRI 2017 workshop [64].
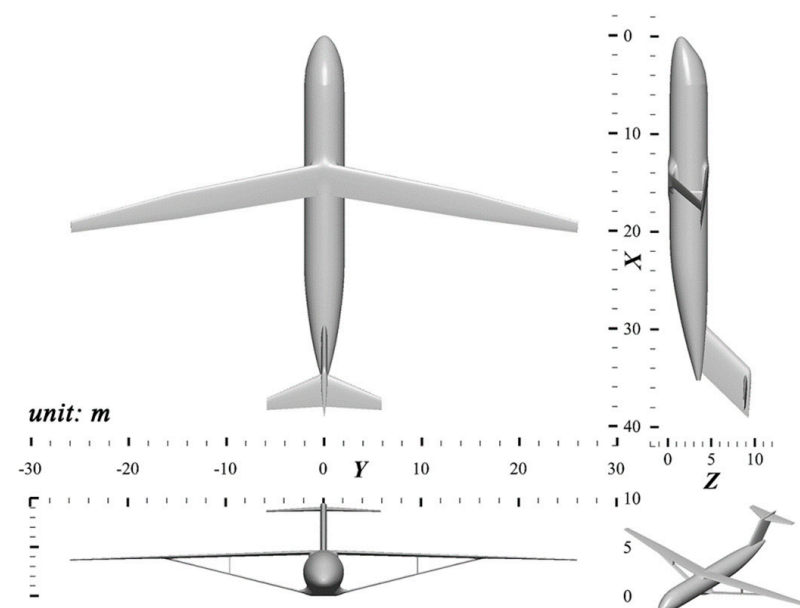

Figure 2. Initial geometry of the entire TBW configuration.

3.3. Computational Grids

We generate a multi-block structured grid for the TBW wing–body–tail configuration using commercial software ANSYS ICEM-CFD with an O-H-type topology and a local

Y-type topology. The volume grid consists of 1264 blocks and has 48.8 million cells, referred to as Level 1 (L1). Following the multigrid approach, the L1 grid is subsequently coarsened twice, resulting in two additional level grids containing 6.1 million cells (referred to as Level 2 or L2) and 760 thousand cells (referred to as Level 3 or L3), respectively. Figure 3 illustrates the global TBW surface mesh, along with the local wing surface mesh for all three level grids. The grid convergence study of this mesh family has been performed in [17], and it has been demonstrated to possess a high level of resolution accuracy. Like the previous work, we still use the L2 grid for optimizations and results discussions with a reasonable computational cost and sufficient accuracy, and the L1 grid is used for post-optimization analysis.

| L1 mesh | L2 mesh | L3 mesh |
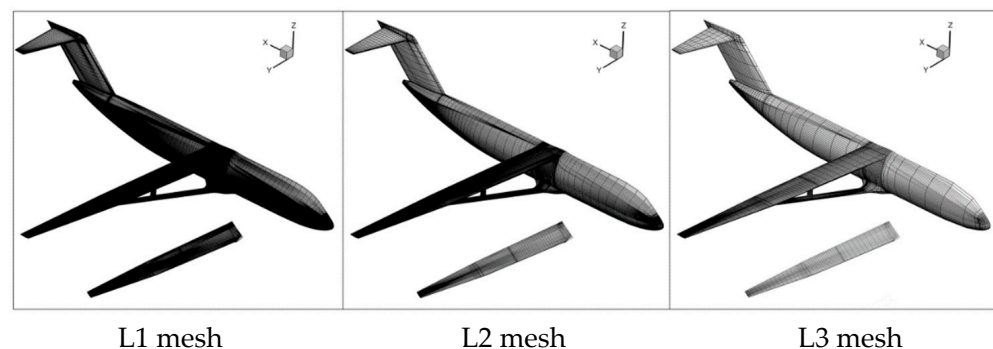
Figure 3. Mesh family of the full TBW configuration.

3.4. Study Cases and Optimization Statement

For the following study cases, we assume that the stability augmentation system and augmented stability controllers will be available for TBW aircraft when entering into service in the near future, such as the time frame of 2035s. It is mainly to state that this aircraft design has sufficient stability reliability.

Study 1: Only Static Stability Margin Effect

In this paper, we change the position of the center of gravity, which is one of the two approaches mentioned above, to achieve the variation in the static stability margin. It is also because the CG position is usually allowed to shift during the conceptual and/or refined design stage, which can be realized to coordinate with other systems, such as those related to payload, fuel, and power [65]. We chose a series of seven CG positions: 5, 10, 15, 20, 25, 30, and 35% MAC, considering that the TBW wing has a smaller MAC compared to the traditional tube-and-wing single-aisle aircraft. Moreover, from the perspective of checking the aerodynamic benefits under both on-design and off-design flight conditions, we evaluate the aerodynamic efficiency improvement under three flight conditions for each CG position. The cruise condition is $M = 0.70$ and $C_L = 0.77$ (a variable of horizontal tail twist is applied to trim under this condition), while the off-design points are the drag divergence condition and the near buffet-onset condition with $M = 0.72$, $C_L = 0.77$, and $M = 0.70$, $C_L = 1.001$, respectively. The study cases are listed in detail in Table 1.

Table 1. Static stability margins design variables only on the initial configuration.

Case	3.1.1	3.1.2	3.1.3	3.1.4	3.1.5	3.1.6	3.1.7
C.G. location (% MAC)	5	10	15	20	25	30	35
	M		**C_L**			**Re**	
Flight Conditions	0.70		0.770			12.30×10^6	
	0.72		0.770			12.65×10^6	
	0.70		1.001			12.30×10^6	

Study 2: Combination of Optimization and Static Stability Margin

A range of seven multipoint aerodynamic design optimization cases is performed to evaluate and analyze the effects, potentials, and tradeoffs of the full TBW wing–body–tail configuration between these research approaches. Each optimization case corresponds to a specific CG position. Table 2 gives a detailed illustration of these cases.

Table 2. Combination of multipoint aerodynamic shape optimizations and static stability margins.

| Case	3.2.1	3.2.2	3.2.3	3.2.4	3.2.5	3.2.6	3.2.7
C.G. location (% MAC)	5	10	15	20	25	30	35
Point		M		C_L		Re	**Weight**
1		0.70		0.770		12.30×10^6	2/3
2		0.72		0.770		12.65×10^6	1/6
3		0.70		1.001		12.30×10^6	1/6

It can be found that each case represents a multipoint aerodynamic shape optimization consisting of the on-design condition, drag divergence condition, and near-buffet condition. These considerations are primarily focused on two key aspects. On the one hand, in our previous research work, one of the most significant conclusions is that this can lead to a comprehensively refined design with attractive aerodynamic performance. On the other hand, these two off-design points are crucial and indispensable aspects in the design of civil transonic aircraft. Both the Civil Aviation Authority (CAA) and Federal Aviation Administration (FAR) have made strict stipulations for these off-design conditions to ensure flight safety. The definition we adopt for drag divergence is based on the SUGAR Phase II study [6]. According to the definition, drag is considered to have increased by fewer than 10 counts as the Mach number increased by 0.02. In this paper, we do not adopt a specific method to estimate the buffet-onset point. We employ the flight point with $M = 0.70$ and $C_L = 1.001$ as the near-buffet condition and as the optimization design point. Furthermore, the SUGAR project's findings in [6] indicate that using $C_L = 1.001$ as a near-buffet flight condition is reasonably justified to a certain extent.

In all of these cases, the objective is to minimize the drag coefficient that is weighted under multi-flight conditions. The variables for optimization design comprise 600 FFD control points (z_j) for the TBW shape, as illustrated by the deep blue points in Figure 4. These control points are distributed as $9 \times 20 \times 2$ points for the wing (spanwise, chordwise, and vertical directions, respectively) and $6 \times 20 \times 2$ points for the main strut. Additionally, there are eight wing sections, excluding the wing root section, along the spanwise direction taken as the wing twist variables (β_k), and five strut sections, excluding the strut root section, along the spanwise direction taken as the strut twist variables (γ_l). Additionally, the angle of attack (α) served as a design variable to constrain the lift, and horizontal tail twist (η) served as a design variable to trim. Furthermore, considering the practical engineering application, the aerodynamic shape optimization design must meet specific requirements for the wing volume and wing structure. This necessitates the inclusion of wing thickness constraints. This paper incorporates a total of 455 thickness constraints distributed across 35 chordwise and 13 spanwise locations, as depicted in Figure 5. Thus, the statement summarizing the optimization cases can be formulated as follows:

$$
\begin{aligned}
&min \quad \sum_{i=1}^{n} W_i C_{Di} \\
&w.r.t. \quad
\begin{cases}
\alpha = \alpha_i, & i = 1, 2, \ldots, n \\
z_j, & j = 1, 2, \ldots, 600 \\
\beta_k, & k = 1, 2, \ldots, 8 \\
\gamma_l, & l = 1, 2, \ldots, 5 \\
\eta
\end{cases} \\
&s.t. \quad
\begin{cases}
C_L = C_{Li}, & i = 1, 2, \ldots, n \\
C_{my\_cruise} = 0 \\
\bar{t}_m \geq \bar{t}_{initial}, & m = 1, 2, \ldots, 455
\end{cases}
\end{aligned}
\tag{3}
$$
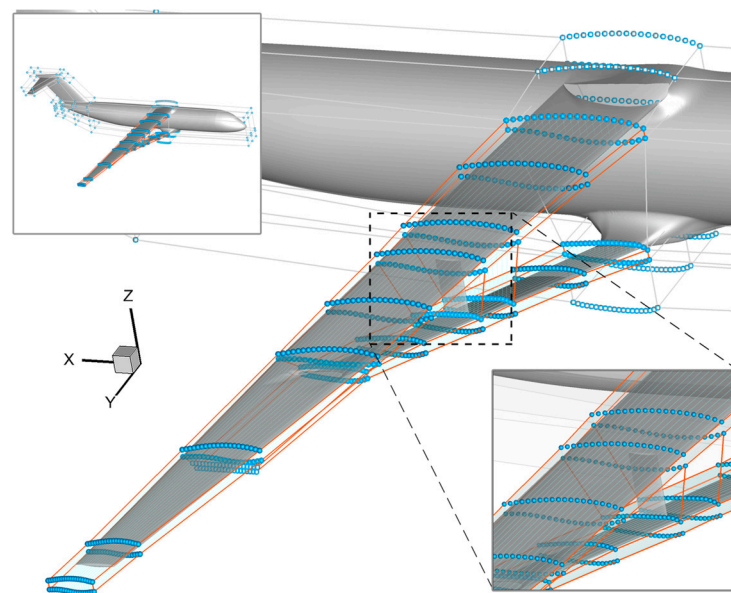
Figure 4. FFD control framework for TBW Aircraft.
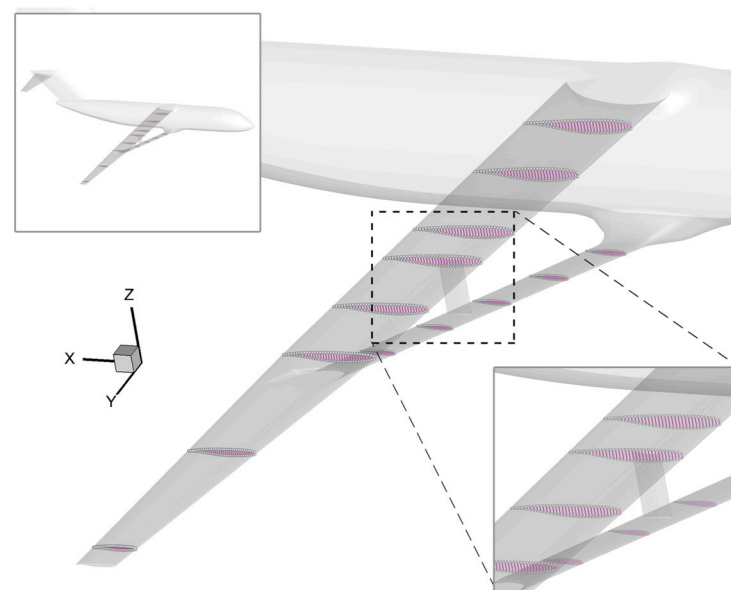
Figure 5. TBW thickness constraints for the optimization.

4. Results and Discussions

4.1. Only Different Static Stability Margins with Initial Configuration

The results of the initial configuration at various CG positions with the L2 grid under cruise conditions are presented in Table 3.

Table 3. Aerodynamic results with different static margins of the initial configuration.

| M	C_L	CG Location (% MAC)	C_D (Counts)	ΔC_D (%)	Kn (%)	η (°)
		5	462.85	/	39.6	−1.307
		10	459.74	−0.67	34.5	−1.004
		15	457.62	−1.13	29.6	−0.700
0.70	0.770	20	455.10	−1.67	24.6	−0.397
		25	454.34	−1.84	19.5	−0.091
		30	452.90	−2.15	15.4	0.209
		35	451.77	−2.39	9.6	0.519

It is evident that the C_D presents a steady decrease with a more aft center of gravity. It decreases from 462.85 counts at the 5% MAC CG position to 451.77 counts at the 35% MAC CG position with a 2.39% drop. This noticeable improvement in aerodynamic performance reflects the tradeoffs between static margin, trim drag, and component load distribution. The drag reduction in the full TBW wing–body–tail configuration has the same trend as those works performed by Lyu et al. about the BWB configuration [65] and Li et al. about the CRM wing–body–tail configuration [32]. Nevertheless, the CRM wing–body–tail configuration, as a traditional tube-and-wing aircraft with a horizontal tail, achieves aerodynamic potential associated with RSS due to the balance between the wing and horizontal tail, resulting in variation in trim drag. In the case of the BWB configuration, which is a tailless aircraft, the aerodynamic benefit associated with RSS is tightly connected with a change in the geometry shape and lift distribution. For the TBW wing–body–tail configuration, as a multi-component complex-geometry aircraft, the effect of RSS on its aerodynamic performance is related to the complex mutual interference among the wing, struts, and tail, meaning that it has to take into consideration the change of the struts lift distribution and the interactions with several junctions other than the balance between the wing and horizontal tail like the CRM configuration.

For this perspective, Figure 6 is presented to further illustrate the variation of aerodynamic features and drag reduction in the initial configuration under cruise conditions with the L2 grid. The top view of the full configuration and main wing (Figure 6a) compares the pressure coefficient (Cp) contour at various CG locations, showing the Cp line distributions vary with small distinction but still have significant changes that will be discussed in detail later with Cp distribution of spanwise sections. In Figure 6b, a front view with the shock surface demonstrates the slight but noticeable change of the shock wave region and its strength. It can be found that the shock is not only affected in the upper wing but also in the fuselage–strut junction and wing–strut junction, which means that the full TBW configuration with the RSS technique has to pay much attention to the strut design. That is also the reason that we add some strut section twist design variables other than the strut shape variables in the optimization cases. The variations in wing, strut, and horizontal tail lift distributions are also presented (Figure 6c). The spanwise lift coefficient (C_l) distribution is employed to show the variation in C_l along with these components more directly. It is evident that both the wing and strut loads decrease, and the tail load is more positive with a more aft CG location, corresponding to the tail twist change for aircraft trim in Table 3. All of these load changes finally lead to a reduction in trim drag, including the wave drag, interference drag, and induced drag. In Figure 6d, we present the comparisons of Cp distribution at nine spanwise sections (six for the wing and three for the main strut). With a more backward CG position, the Cp distribution in sections A, G, and H have a lower negative Cp peak in the leading edge; sections B–F have a similar trend: a lower negative Cp peak in the leading edge and a weaker adverse pressure gradient; section I is slightly affected only in the lower surface.

Table 4 presents the results of the initial configuration at various CG positions with the L2 grid under off-design conditions. The C_D also shows a steady decline with a more rear CG. That of the drag divergence condition falls from 475.96 counts at the 5% MAC CG to 461.63 counts at the 35% MAC CG with a 3.01% drop, while that with the near-buffet condition falls from 693.91 counts at the 5% MAC CG to 657.56 counts at the 35% MAC CG with a 5.24% drop. The decreasing amplitudes of drag from 5% MAC CG to 35% MAC CG under off-design conditions are similar to that of the on-design condition, and the near-buffet condition has a bigger drag reduction. Moreover, the aerodynamic performances of the initial configuration at various CG positions under off-design conditions are illustrated in Figures 7 and 8. Both the variations in aerodynamic features shown in these figures are in accordance with the observations made in the cruise condition.
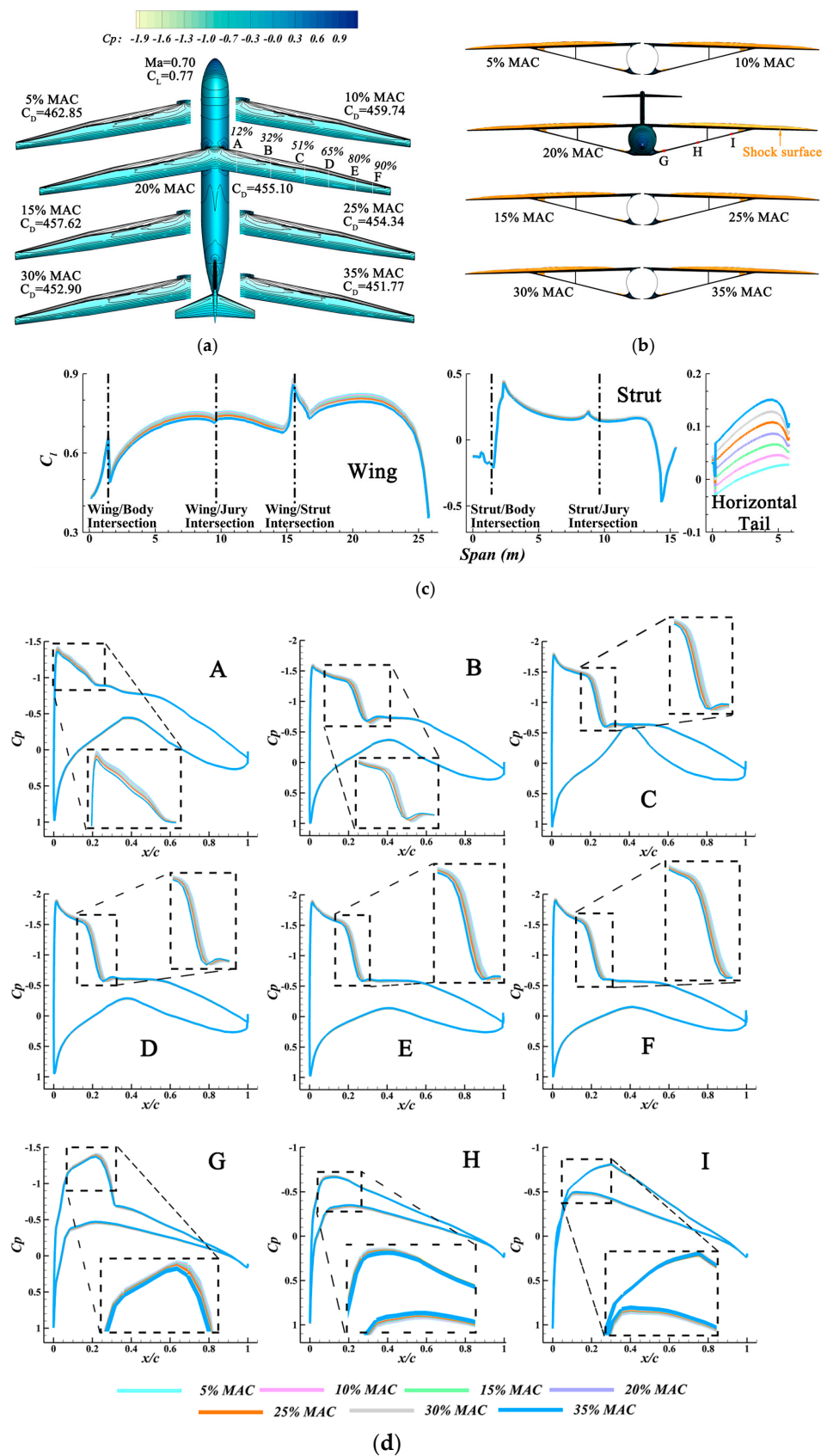
Figure 6. Aerodynamic performance with different static margins under cruise conditions. (**a**) Top view, (**b**) front view, (**c**) spanwise lift coefficient distribution, (**d**) sectional pressure coefficient contours (the subfigures are the locally enlarged pressure coefficient contours).
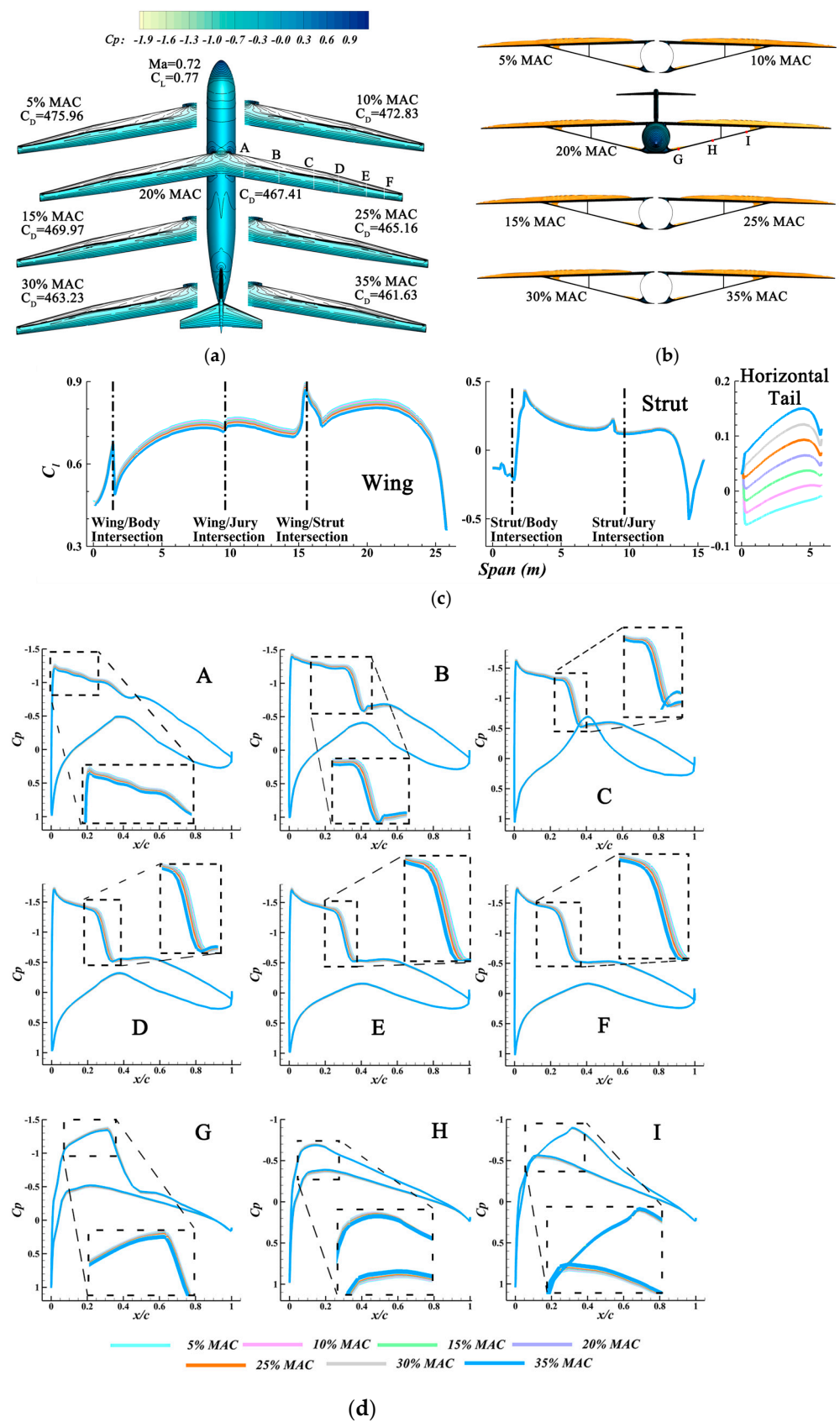
Figure 7. Aerodynamic performance with different static margins under drag divergence conditions. (**a**) Top view, (**b**) front view, (**c**) spanwise lift coefficient distribution, (**d**) sectional pressure coefficient contours (the subfigures are the locally enlarged pressure coefficient contours).
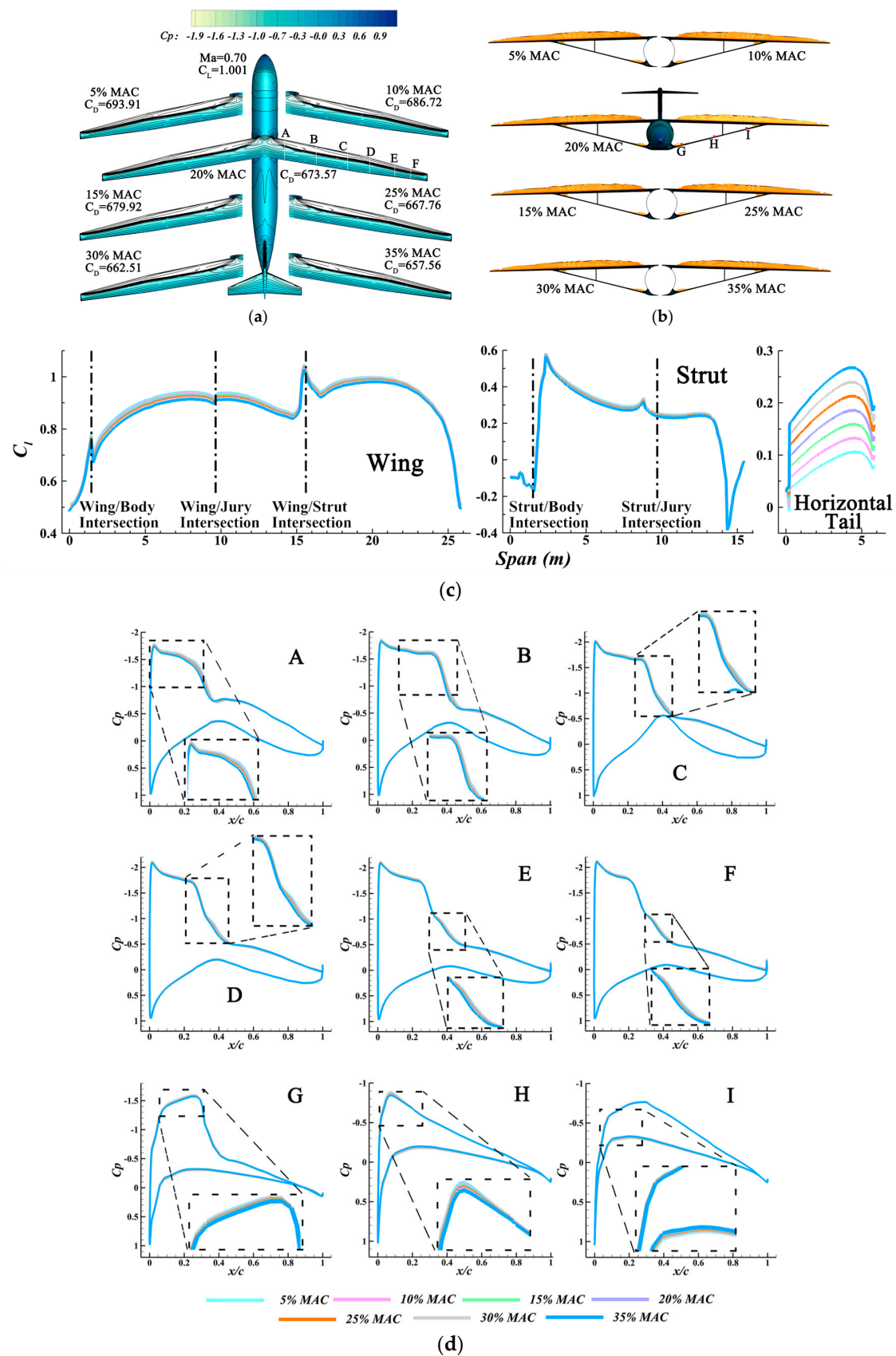
Figure 8. Aerodynamic performance with different static margins under the near buffet-onset condition. (**a**) Top view, (**b**) front view, (**c**) spanwise lift coefficient distribution, (**d**) sectional pressure coefficient contours (the subfigures are the locally enlarged pressure coefficient contours).

Table 4. Aerodynamic results of initial configuration under off-design conditions.

M	C_L	CG Location (% MAC)	C_D (Counts)	ΔC_D (%)
		5	475.96	/
		10	472.83	−0.66
		15	469.97	−1.26
0.72	0.770	20	467.41	−1.80
		25	465.16	−2.27
		30	463.23	−2.67
		35	461.63	−3.01
		5	693.91	/
		10	686.72	−1.04
		15	679.92	−2.02
0.70	1.001	20	673.57	−2.93
		25	667.76	−3.77
		30	662.51	−4.53
		35	657.56	−5.24

In Figure 9, we provide the local aerodynamic features of the initial configuration at different CG positions under cruise conditions with two different spanwise positions (A means the spanwise position is 5.7 m, and B means the spanwise position is 12.6 m). It can help understand the variations in interactions at the wing–strut regions when only the static margins change, corresponding to the explanations in Figure 6. Additionally, it further indicates the trend of slight shock variation in the upper wing and spatial regions.
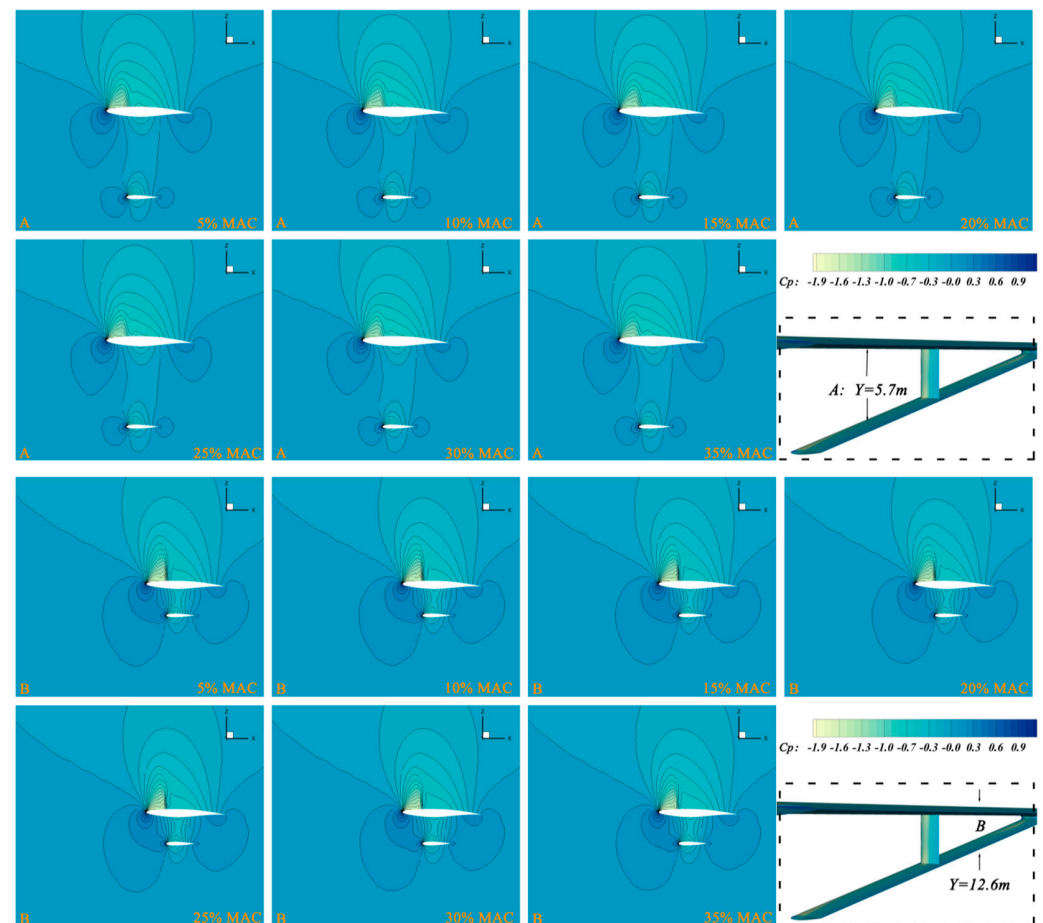
Figure 9. Local aerodynamic analysis in wing–struts region with different static margins under cruise condition.

Overall, in this study 1 only with different static stability margins, for the initial configuration without any shape modification or optimization, it has a big C_D and local strong adverse pressure gradient under different flight conditions. However, the application of RSS indicates that TBW aircraft could have attractive potential in terms of better aerodynamic performance. Additionally, the explanation for drag reduction is twofold: on the one hand, the lift shifts from wing/truss to the tail due to the rear CG, which leads the weakened shock strength of the wing/truss by the load reduction; on the other hand, when shifting load to the tail, the trim drag is reduced, where the induced drag of the tail is decreased due to less downforce. More importantly, it can be found that the multi-components, such as the wing, tail, struts, and intersections, are all affected by this technique, highlighting the significance of high-fidelity exploration and the refined comprehensive aerodynamic design for the entire TBW configuration.

4.2. Combination of Aerodynamic Shape Optimizations and Static Stability Margins

Based on the analysis of aerodynamic performances with the RSS approach and its effects on the multiple components in Section 4.1, it inspires us to perform a refined multi-point aerodynamic shape optimization to further explore the potentials and evaluate the associated tradeoffs. The discussions in this section pertain to the optimization problems of Study 2, as outlined in Section 3.4. Figure 10 illustrates the optimization history of weighted C_D and feasibility with different cases. Feasibility, in this context, is defined as the deviation between the Karush–Kuhn–Tucker (KKT) condition and the current condition of the Lagrangian function in the SQP algorithm. For all the optimization cases, there are around 50 iterations performed with the L2 grid. The weighted C_D exhibits minimal variation during the final iteration, remaining under 0.2 counts, indicating that the optimization has converged. The feasibility value ultimately reaches approximately 1×10^{-5}, demonstrating that the optimization result satisfactorily adheres to the imposed constraints.
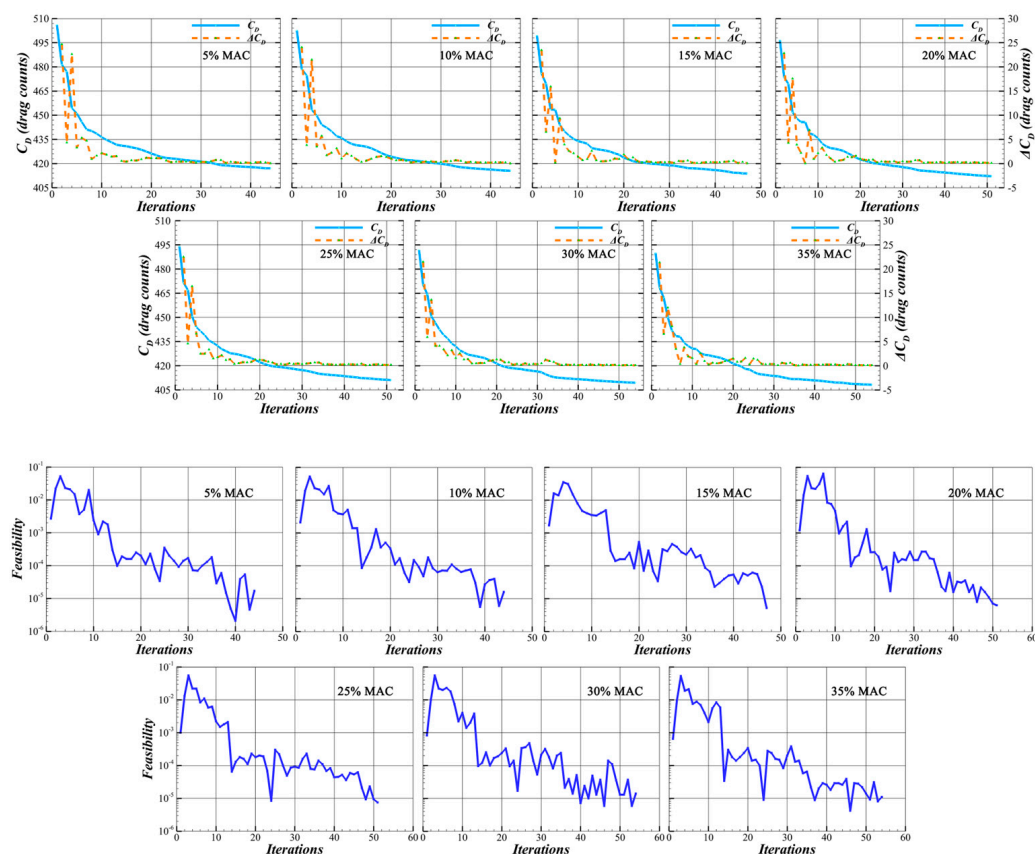

Figure 10. Optimization history for study 2.

Table 5 summarizes the results of the optimized configurations at various CG positions with the L2 grid under cruise conditions (5_35% MAC means the optimized configuration at 5% CG but simulated at 35% CG). On the one hand, it is obvious that each optimized geometry at a certain CG has a considerable and significant drag reduction with the shape modification approach compared to the initial configuration. On the other hand, when the CG location shifts backward, the C_D of the optimized configurations still presents a steady fall. It decreases from 400.35 counts at the 5% MAC CG position to 391.84 counts at the 35% MAC CG position, with a 2.13% drop. This comprehensive improvement in aerodynamic performance demonstrates the significant advantages achieved by integrating the RSS method with the aerodynamic shape optimization technique.

Table 5. Aerodynamic results with different static margins of the optimized configurations.

M	C_L	CG Location (% MAC)	C_D (Counts)	ΔC_D (%)	Kn (%)	η (°)
0.70	0.770	5	400.35	/	42.6	−1.872
		5_35% MAC	397.75	−0.65	12.6	−0.072
		10	398.99	−0.34	37.5	−1.615
		15	397.46	−0.72	32.5	−1.344
		20	395.96	−1.10	27.5	−1.103
		25	394.69	−1.41	22.5	−0.849
		30	393.14	−1.80	17.4	−0.595
		35	391.84	−2.13	12.3	−0.366

The detailed discussions of aerodynamic features and drag reduction under cruise conditions with the L2 grid are illustrated in Figure 11, which includes the comparisons between the initial and optimized configurations with 20% MAC CG location and the variations of all the optimized configurations at different CG positions.

Firstly, the top view of the full configuration in Figure 11a compares the Cp contour of the initial (left) and optimized (right) configurations at 20% MAC CG location, clearly showing that the Cp lines are distributed more evenly, and the upper surface has a gentle, weak pressure gradient in the optimized configuration, which has the same trend with the multipoint optimization works conducted previously [17]. The top view of the other main wings compares the Cp contour of different optimized configurations, displaying the distinction of local pressure gradient variations that will be discussed in detail later with the Cp distribution and airfoils of different spanwise sections.

Secondly, in Figure 11b, a front view of the full configuration presents the change in the shock wave region and strength at 20% MAC CG location. It is evident that, with shape optimization, the vast majority of shock waves of the initial configuration have been eliminated, particularly in the junction parts. The main difference between each optimized geometry is the weak shock region in the outboard wing.

Moreover, Figure 11c provides comparisons of the wing, strut, and horizontal tail lift distributions for all of the configurations. Compared to the initial model at 20% MAC CG location, the optimized one has a lower horizontal tail load, while the wing–strut part tends to load change to achieve a reduction in induced drag, like the multipoint optimization in [17]. All of the optimized configurations have a similar load change trend as those in the initial models shown in Section 4.1.

Furthermore, the Cp distributions and foils at nine spanwise sections for various configurations are compared in Figure 11d (5% MAC_Opt_35%C means the optimized configuration at 5% CG but simulated at 35% CG). On the one hand, only at the 20% MAC CG position do the Cp distributions in wing sections A-D of the optimized model have similar characteristics: a lower negative Cp peak in the leading edge, a couple of weak pressure gradients (this similar trend can be found in other multipoint optimization cases [66,67]), and a smooth pressure recovery. The wing sections E and F have a Cp distribution of a lower negative Cp peak in the leading edge, followed by pressure recovery and a second acceleration, resulting in a second weak compression near the middle chord. While strut sections G and I have a lower suction peak in the leading edge with a smooth pressure recovery, and strut section H has a lower suction peak in the leading edge, a weaker adverse

pressure gradient, and pressure recovery. On the other hand, with a more rear CG position, the variations in *Cp* distributions are mainly reflected in the aspects of the suction peak and the magnitude of the pressure gradient.
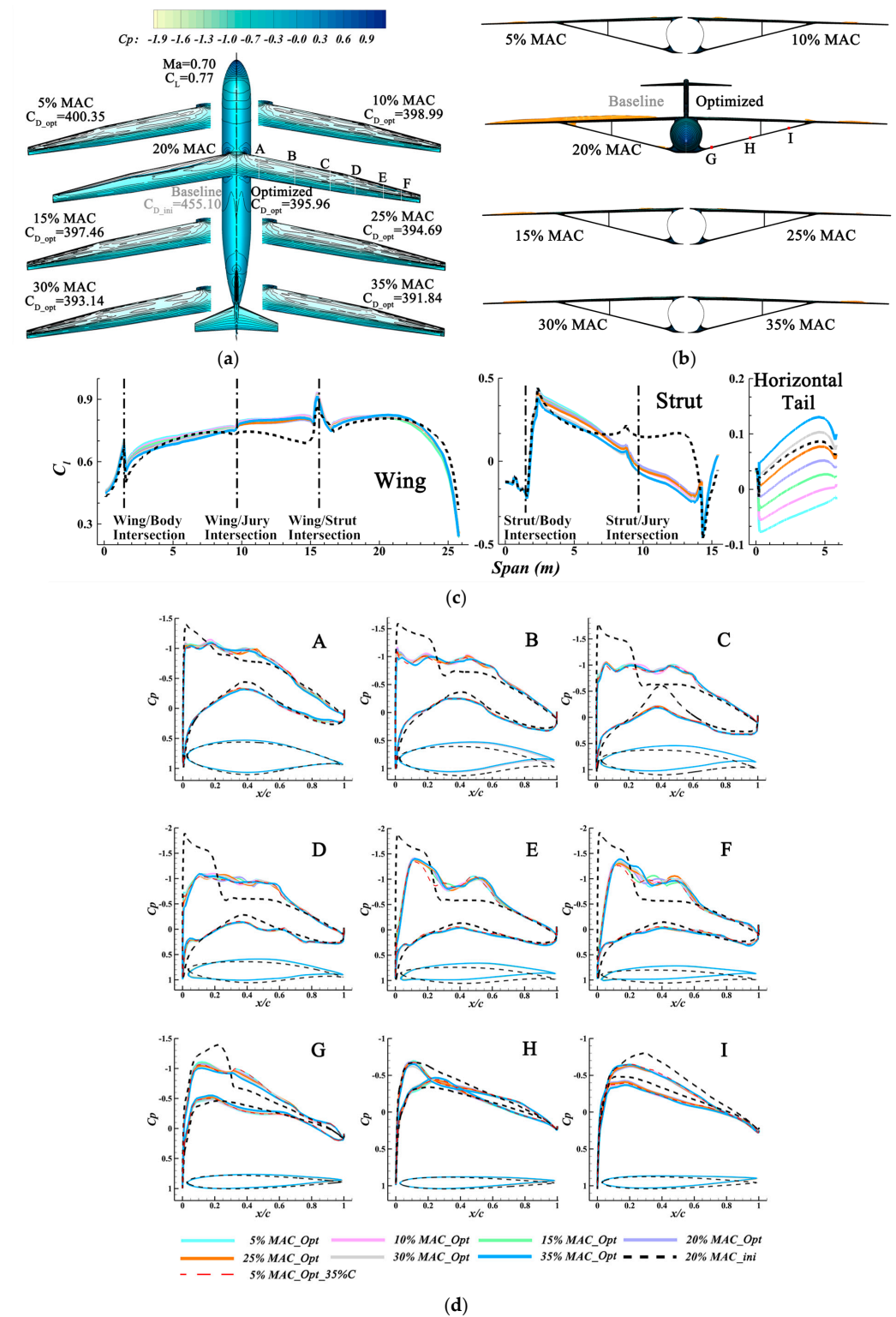
Figure 11. Aerodynamic performance of optimized configurations under cruise conditions. (**a**) Top view, (**b**) front view, (**c**) spanwise lift coefficient distribution, (**d**) sectional pressure coefficient contours (the upper part is the sectional pressure coefficient contour, and the lower part is the sectional airfoil).

In addition, the results for the optimized configurations at various CG positions with the L2 grid under off-design conditions are summarized in Table 6. Still, the C_D of these conditions shows a gradual decrease with a more backward CG. That of the drag divergence condition declines from 409.48 counts at the 5% MAC CG position to 399.58 counts at the 35% MAC CG position, with a 2.42% drop, while the near-buffet condition falls from 491.65 counts at the 5% MAC CG position to 481.23 counts at the 35% MAC CG position with a 2.12% drop. It is unlike the findings in study 1, where the off-design conditions of the initial model exhibit a greater extent of drag reduction compared to the on-design condition. The drag reduction achieved by all the optimized configurations with a rear CG under the off-design conditions is comparable to that observed under cruise conditions. From this perspective, it reflects that multipoint shape optimization has the ability to provide a suitable optimized baseline geometry that has a good performance under various flight conditions. Consequently, with the application of the RSS approach, it becomes fairer in terms of assessing and highlighting aerodynamic potential and benefits based on shape optimization.

Table 6. Aerodynamic results of the optimized configurations under off-design conditions.

M	C_L	CG Location (% MAC)	C_D (Counts)	ΔC_D (%)
0.72	0.770	5	409.48	/
		5_35% MAC	405.74	−0.91
		10	407.13	−0.57
		15	405.59	−0.95
		20	404.24	−1.28
		25	402.86	−1.62
		30	401.34	−1.99
		35	399.58	−2.42
0.70	1.001	5	491.65	/
		5_35% MAC	483.39	−1.68
		10	490.36	−0.26
		15	487.80	−0.78
		20	485.15	−1.32
		25	484.65	−1.42
		30	483.08	−1.74
		35	481.23	−2.12

In addition, Figures 12 and 13 present the aerodynamic features of the optimized configurations at various CG positions under off-design conditions. On the one hand, it shows the more evident elimination of shock and variations in Cp distribution between the initial and optimized configurations. On the other hand, the differences among these optimized configurations are similar to that observed under cruise conditions.

The local aerodynamic features of various optimized configurations under cruise conditions are shown in Figure 14. On the one side, compared to the initial configuration shown in Figure 9, all of the optimized configurations exhibit a bigger throat space (the region between the lower surface of the wing and the upper surface of the strut) that improves the pressure distribution and weakens the shock strength, which is in agreement with the "convergent-divergent nozzle" effect that was discussed in our previous work [17] and the study conducted by Ko et al. [68]. On the other side, the different static margins show a more evident effect on the variations in pressure distribution in the volume, especially in the shock wave region of the upper wing.

For now, it is obvious that the optimized configuration with the 35% MAC CG location has a better aerodynamic performance and a greater potential for drag reduction. Therefore, we based this model on the L1 grid to conduct a more precise analysis and evaluate some other off-design flight conditions, as shown in Table 7, which also presents the performance comparison between the initial and optimized configurations (where Ori and Opt mean

the initial configuration and the optimized configuration, respectively, and ΔC_D (%) and $\Delta M*L/D$ (%) mean aerodynamic performance variation by percentage).
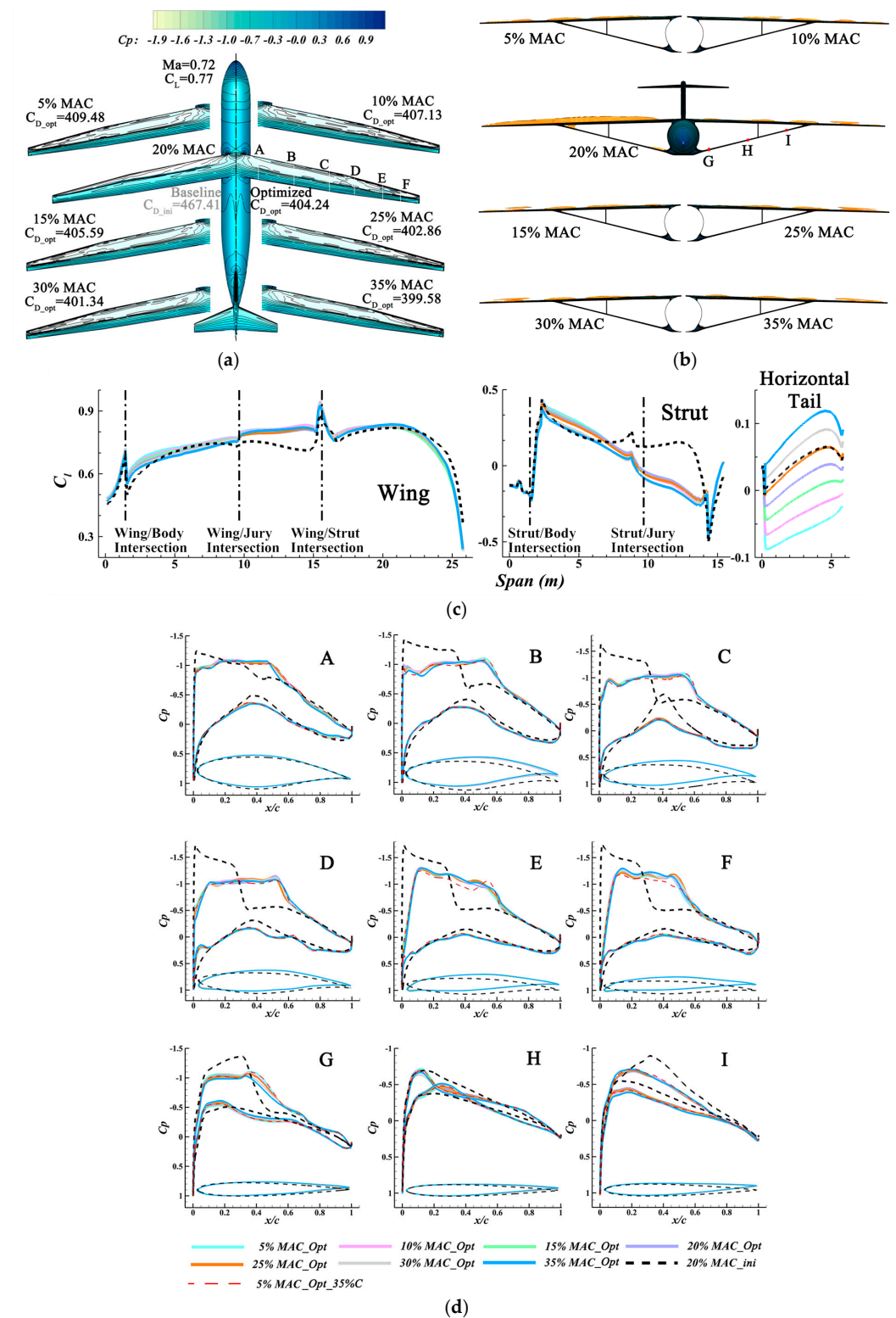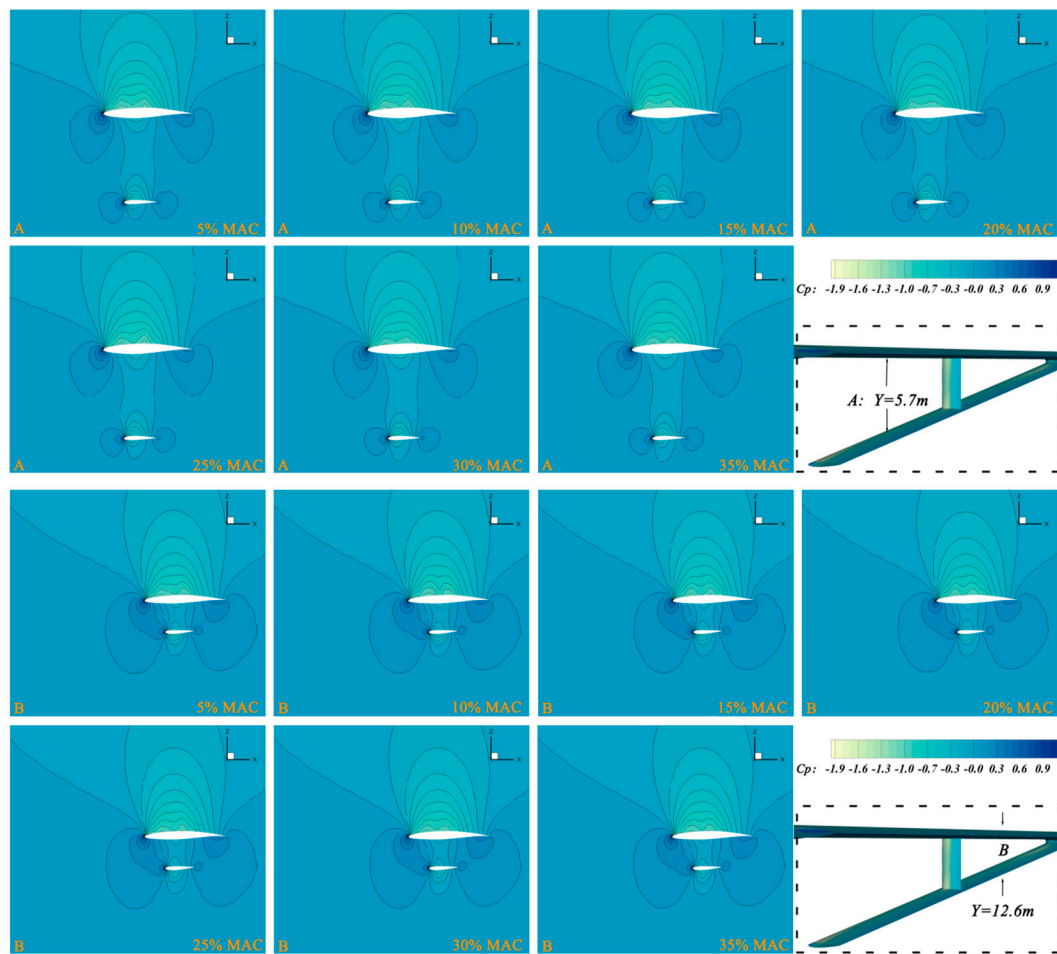

Figure 12. Aerodynamic performance of optimized configurations under drag divergence conditions. (**a**) Top view, (**b**) front view, (**c**) spanwise lift coefficient distribution, (**d**) sectional pressure coefficient contours (the upper part is the sectional pressure coefficient contour, and the lower part is the sectional airfoil).
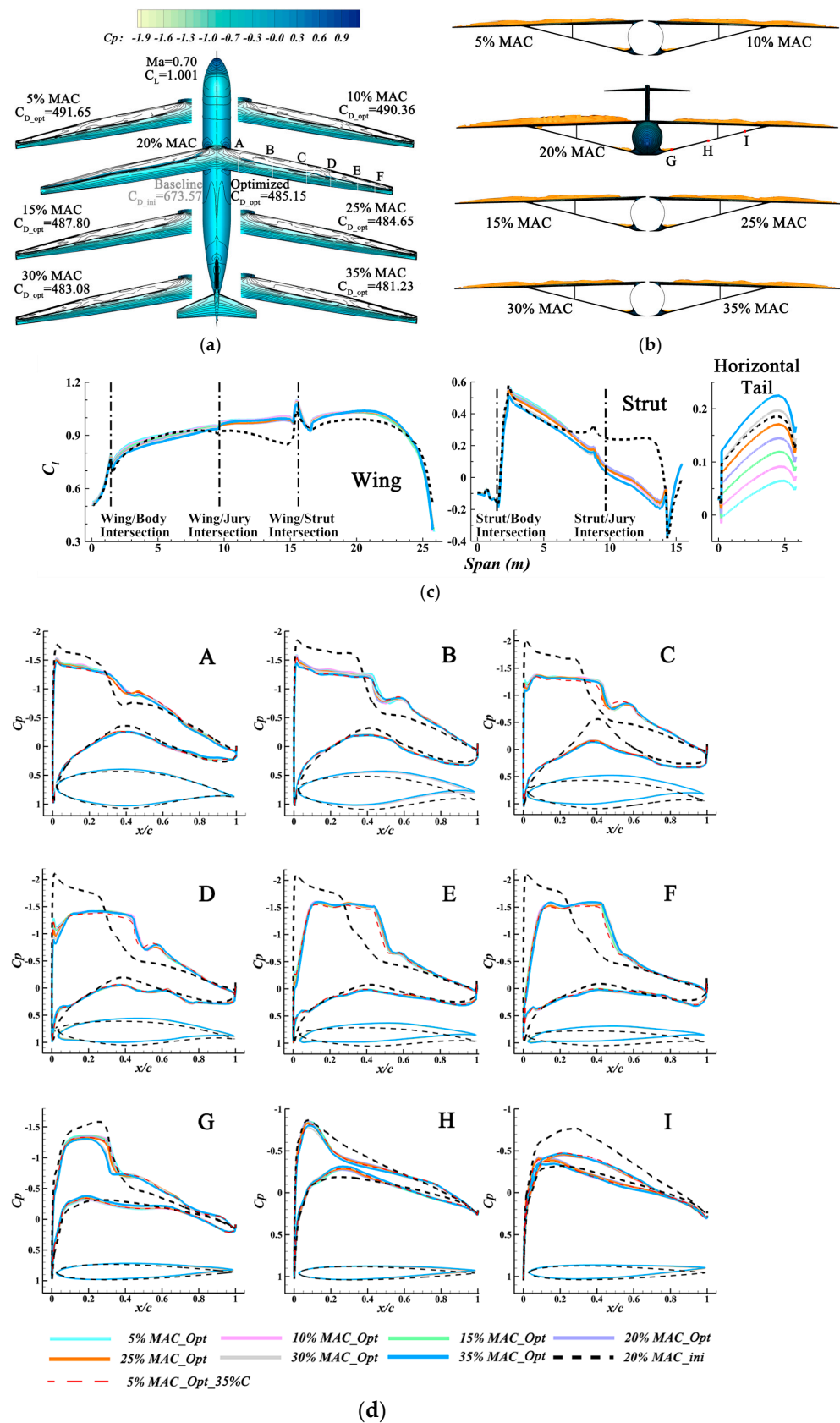
Figure 13. Aerodynamic performance of optimized configurations under the near buffet-onset conditions. (**a**) Top view, (**b**) front view, (**c**) spanwise lift coefficient distribution, (**d**) sectional pressure coefficient contours (the upper part is the sectional pressure coefficient contour, and the lower part is the sectional airfoil).

Figure 14. Local aerodynamic analysis in wing–struts region of optimized geometries under cruise conditions.

Table 7. Aerodynamic performance of optimization configuration with 35% MAC CG position and the performance comparison between the initial and optimized configurations.

	M	0.67	0.68	0.70	0.72	0.73	0.70	0.70	0.70
	C_L	0.770	0.770	0.770	0.770	0.770	0.720	0.820	1.001
Ori	C_D(counts)	362.11	363.40	367.75	377.58	385.86	343.51	397.45	570.45
	*M*L/D*	14.25	14.41	14.66	14.68	14.57	14.67	14.44	12.28
Opt	C_D(counts)	310.84	312.07	314.50	322.85	344.33	303.59	327.98	403.78
	ΔC_D (%)	−14.16	−14.12	−14.48	−14.49	−10.76	−11.62	−17.48	−29.22
	*M*L/D*	16.60	16.78	17.14	17.17	16.32	16.60	17.50	17.35
	$\Delta M*L/D$ (%)	16.49	16.45	16.93	16.95	12.06	13.15	21.18	41.28

The C_D under cruise conditions is 314.50 counts with an *L/D* of 24.48, and the *M*L/D* is 17.14. For the condition of *M* = 0.72, the C_D is 322.85 counts, and it is 8.35 counts larger than that of the *M* = 0.70 condition, which means that it can meet the drag divergence requirement. For the C_L = 1.001 condition, it has a well-behaved aerodynamic performance with an *M*L/D* of 17.35, which shows that it has good aerodynamic behavior and a similar aerodynamic efficiency compared to *M* = 0.70 and *M* = 0.72 conditions. While other off-design conditions also present a high level of aerodynamic efficiency, demonstrating this configuration with the combined approaches of multipoint aerodynamic shape optimization and RSS is a comprehensive refined design with attractive aerodynamic performance.

5. Conclusions

In this paper, based on a high-fidelity solver for a full complex TBW configuration, we have evaluated the aerodynamic benefits via the application of relaxed static stability only and investigated comprehensive and robust aerodynamic designs with the combination of relaxed static stability and the aerodynamic shape optimization method. To study the effects of the static stability margin, we performed research on the baseline geometry under both on-design and off-design conditions. This allows us to assess the influences on the multi-components, such as the wing, tail, struts, and intersections. To achieve refined designs with various aerodynamic approaches, we conduct seven multipoint aerodynamic design optimizations to further explore the potential for drag reduction and improved aerodynamic performance.

In Study 1, with only different static stability margins without any shape modification or optimization, the C_D under cruise conditions has a 2.39% drop with a more rear CG position from 5% MAC to 35% MAC. As for the off-design conditions, the C_D of the drag divergence condition falls with a 3.01% drop, and that under near-buffet conditions has a 5.24% drop. It indicates that, just for the initial full TBW aircraft, it still has attractive aerodynamic potential and better performance with the application of RSS under different flight conditions. Moreover, we have observed and discussed that the multi-components, such as wing, tail, struts, and intersections, are all affected by this active control technique, proving the need for higher-fidelity exploration and refined comprehensive aerodynamic design for a full complex TBW configuration.

Then, in Study 2, we perform seven multipoint aerodynamic design optimization cases with respect to 600 wing–strut shape variables and 13 wing–strut twist variables, subject to lift coefficient, trim, and thickness constraints. Under cruise conditions, compared to the initial configuration, all of the optimized configurations, on the one hand, exhibit a slightly weakened shock and show a more even Cp line distribution. Additionally, they have a lower horizontal tail load, and all of these load changes with the wing/strut/tail parts lead to a reduction in drag, including wave drag, interference drag, and induced drag. On the other hand, the C_D of the optimized configurations presents a steady fall with a more aft CG position. It decreases from 400.35 counts at the 5% MAC CG position to 391.84 counts at the 35% MAC CG position with a 2.13% drop. As for the off-design conditions, when moving the CG position from 5% MAC to 35% MAC, the C_D of the drag divergence condition declines from 409.48 counts to 399.58 counts with a 2.42% drop, and the near-buffet condition falls from 491.65 counts to 481.23 counts with a 2.12% drop. Considering that the optimized configuration with a 35% MAC CG location has better aerodynamic performance, we based this model on the finest grid (48.8 million cells) to conduct a more precise analysis, the C_D under on-design conditions is 314.50 counts, and its L/D and $M*L/D$ is 24.48 and 17.14, respectively. While for the conditions of $M = 0.72$ and $C_L = 1.001$, the aerodynamic efficiency of $M*L/D$ is 17.17 and 17.35, respectively. Moreover, some more off-design points are evaluated, and the results also present a high-level aerodynamic efficiency.

Overall, these study results highlight the fact that to realize aerodynamic potential and performance improvement in a complex TBW configuration, the combination of the multipoint aerodynamic shape optimization method and the RSS active control approach has an impressive effect on comprehensively refined aerodynamic shape optimization, and it is beneficial to further explore the detailed aerodynamic features.

Author Contributions: Conceptualization, L.L., L.Q., J.X. and J.B.; methodology, L.L. and L.Q; software, L.L.; validation, L.L., L.Q. and J.X.; formal analysis, L.L., L.Q., J.X. and J.B.; investigation, L.L., L.Q., J.X. and J.B.; resources, L.L., L.Q., J.X. and J.B.; data curation, L.L., L.Q., J.X. and J.B.; writing, original draft preparation, L.L., L.Q., J.X. and J.B.; writing, review and editing, L.L., L.Q., J.X. and J.B.; visualization, L.L.; supervision, L.Q., J.X. and J.B.; project administration, L.Q., J.X. and J.B. All authors have read and agreed to the published version of the manuscript.

Data Availability Statement: The data that support the findings of this study are available from the corresponding author upon reasonable request.

Conflicts of Interest: The authors declare that they have no known competing financial interest or personal relationships that could have influence the work reported in this paper.

Nomenclature

α	angle of attack
β_k	wing twist angle
γ_l	strut twist angle
η	horizontal tail twist angle
a	local sound speed
c	thrust specific fuel consumption
C_D	drag coefficient
C_L	lift coefficient
$C_{L\alpha}$	derivative of C_L with respect to α
C_{my}	pitching moment coefficient
$C_{m\alpha}$	derivative of C_{my} with respect to α
C_p	pressure coefficient
K_n	static longitudinal stability margin
L/D	lift-to-drag ratio
M	Mach number
MAC	mean aerodynamic chord
Re	Reynolds number
t/c	thickness-to-chord ratio
$\bar{t}_m$	thickness constraints
x_n	locations of the neutral point
x_{CG}	location of the center of gravity
z_j	FFD control points

References

1. Chen, Z.L.; Zhang, M.H.; Chen, Y.C.; Sang, W.M.; Tan, Z.G.; Li, D.; Zhang, B.Q. Assessment on critical technologies for conceptual design of blended-wing-body civil aircraft. *Chin. J. Aeronaut.* **2019**, *32*, 1797–1827. [CrossRef]
2. Karpuk, S.; Ma, Y.; Elham, A. Design Investigation of Potential Long-Range Hydrogen Combustion Blended Wing Body Aircraft with Future Technologies. *Aerospace* **2023**, *10*, 566. [CrossRef]
3. Lee, D.S.; Fahey, D.W.; Skowron, A.; Allen, M.R.; Burkhardt, U.; Chen, Q.; Doherty, S.J.; Lim, L.L.; Freeman, S.; Forster, P.M.; et al. The Contribution of Global Aviation to Anthropogenic Climate Forcing for 2000 to 2018. *Atmos. Environ.* **2021**, *244*, 117834. [CrossRef] [PubMed]
4. Bradley, M.K.; Droney, C.K. *Subsonic Ultra Green Aircraft Research: Phase I Final Report*; CR-2011-216847; NASA: Washington, DC, USA, 2011.
5. Bradley, M.K.; Droney, C.K. *Subsonic Ultra Green Aircraft Research Phase II: N + 4 Advanced Concept Development*; CR-2012-217556; NASA: Washington, DC, USA, 2012.
6. Bradley, M.K.; Droney, C.K.; Allen, T.J. *Subsonic Ultra Green Aircraft Research: Phase II—Volume I—Truss Braced Wing Design Exploration*; CR-2015-218704; NASA: Washington, DC, USA, 2015; Volume I.
7. Bradley, M.K.; Droney, C.K. *Subsonic Ultra Green Aircraft Research: Phase II—Volume II—Hybrid Electric Design Exploration*; CR–2015-218704; NASA: Washington, DC, USA, 2015; Volume II.
8. International Air Transport Association. *IATA Technology Roadmap*, 4th ed.; International Air Transport Association: Montreal, QC, Canada, 2013.
9. International Air Transport Association. *IATA Technology Roadmap to 2050*; International Air Transport Association: Montreal, QC, Canada, 2019.
10. International Civil Aviation Organization (ICAO). *Consolidated Statement of Continuing ICAO Policies and Practices Related to Environmental Protection—Global Market-Based Measure (MBM) Scheme*; International Civil Aviation Organization (ICAO): Montreal, QC, Canada, 2016.
11. ICAO. *37th Assembly Working Papers, A37-WP/402*; ICAO: Montreal, QC, Canada, 2010.
12. Innovation Takes off, Clean Sky European Research for Aeronautics. *Clean Sky Book*; Le Cherche Midi: Paris, France, 2016.

13. Krein, A.; Williams, G. Flightpath 2050: Europe's vision for aeronautics. Innovation for Sustainable Aviation in a Global Environment. In In Proceedings of the Sixth European Aeronautics Days, Madrid, Spain, 30 March–1 April 2011.

14. Abbas, A.; De Vicente, J.; Valero, E. Aerodynamic Technologies to Improve Aircraft Performance. *Aerosp. Sci. Technol.* **2013**, *28*, 100–132. [CrossRef]

15. Bravo-Mosquera, P.D.; Catalano, F.M.; Zingg, D.W. Unconventional Aircraft for Civil Aviation: A Review of Concepts and Design Methodologies. *Prog. Aerosp. Sci.* **2022**, *131*, 100813. [CrossRef]

16. Cavallaro, R.; Demasi, L. Challenges, Ideas, and Innovations of Joined-Wing Configurations: A Concept from the Past, an Opportunity for the Future. *Prog. Aerosp. Sci.* **2016**, *87*, 1–93. [CrossRef]

17. Li, L.; Bai, J.Q.; Qu, F. Multipoint Aerodynamic Shape Optimization of a Truss-Braced-Wing Aircraft. *J. Aircr.* **2022**, *59*, 1179–1194. [CrossRef]

18. Gundlach, J.F.; Tetrault, P.-A.; Gern, F.H.; Naghshineh-Pour, A.H.; Ko, A.; Schetz, J.A.; Mason, W.H.; Kapania, R.K.; Grossman, B.; Haftka, R.T. Multidisciplinary design optimization of a strut-braced wing transonic transport. In Proceedings of the 38th AIAA Aerospace Sciences Meeting and Exhibit, Reno, NV, USA, 10–13 January 2000.

19. Gur, O.; Bhatia, M.; Schetz, J.A.; Mason, W.H.; Kapania, R.K.; Mavris, D.T. Design optimization of a truss-braced-wing transonic transport aircraft. *J. Aircr.* **2010**, *47*, 1907–1917. [CrossRef]

20. Mallik, W.; Kapania, R.K.; Schetz, J.A. Effect of flutter on the multidisciplinary design optimization of truss-braced-wing aircraft. *J. Aircr.* **2015**, *52*, 1858–1872. [CrossRef]

21. Bhatia, M.; Kapaniay, R.K.; Haftka, R.T. Structural and aeroelastic characteristics of truss-braced wings: A Parametric Study. *J. Aircr.* **2012**, *49*, 302–310. [CrossRef]

22. Nguyen, N.; Fugate, J.; Xiong, J.T.; Kaul, U. Flutter analysis of the transonic truss-braced wing aircraft using transonic correction. In Proceedings of the AIAA SciTech 2019 Forum, San Diego, CA, USA, 7–11 January 2019.

23. Chau, T.; Zingg, D.W. Aerodynamic Optimization and Fuel Burn Evaluation of a Transonic Strut-Braced-Wing Single-Aisle Aircraft. *J. Aircr.* **2023**, 1–21. [CrossRef]

24. Lee, K.; Kang, S. Propulsion System Modeling and Reduction for Conceptual Truss-Braced Wing Aircraft Design. *Int. J. Aeronaut. Space Sci.* **2017**, *18*, 651–661. [CrossRef]

25. Ting, E.; Reynolds, K.; Nguyen, N.; Totah, J. Aerodynamic analysis of the truss-braced wing aircraft using vortex-lattice superposition approach. In Proceedings of the 32nd AIAA Applied Aerodynamics Conference, Atlanta, GA, USA, 16–20 June 2014.

26. Gur, O.; Schetz, J.A.; Mason, W.H. Aerodynamic considerations in the design of truss-braced-wing aircraft. *J. Aircr.* **2011**, *48*, 919–939. [CrossRef]

27. Demasi, L.; Monegato, G.; Cavallaro, R.; Rybarczyk, R. Minimum induced drag conditions for truss-braced wings. *AIAA J.* **2018**, *56*, 4669–4684. [CrossRef]

28. Gagnon, H.; Zingg, D.W. Euler-Equation-Based Drag Minimization of Unconventional Aircraft Configurations. *J. Aircr.* **2016**, *53*, 1361–1371. [CrossRef]

29. Secco, N.R.; Martins, J.R.R.A. RANS-Based Aerodynamic Shape Optimization of a Strut-Braced Wing with Overset Meshes. *J. Aircr.* **2019**, *56*, 217–227. [CrossRef]

30. Newman, B.; Buttrill, C. Conventional flight control for an aeroelastic, relaxed static stability high-speed transport. In Proceedings of the Guidance, Navigation, and Control Conference, Baltimore, MD, USA, 7–10 August 1995.

31. Urie, D.M.; Reaser, J.S. Aerodynamic development of a small horizontal tail for an active control relaxed stability transport application. In Proceedings of the 5th Atmospheric Flight Mechanics Conference for Future Space Systems, Boulder, CO, USA, 6–8 August 1979.

32. Li, L.; Bai, J.Q.; Guo, T.B.; Chen, S. Aerodynamic Optimization Design for Civil Aircraft Considering Relaxed Static Stability. *Acta Aeronaut. Astronaut. Sin.* **2017**, *38*, 121112. (In Chinese)

33. Zhang, M.H.; Chen, Z.L.; Tan, Z.G.; Gu, W.T.; Li, D.; Yuan, C.S.; Zhang, B.Q. Effects of stability margin and thrust specific fuel consumption constrains on multi-disciplinary optimization for blended-wing-body design. *Chin. J. Aeronaut.* **2019**, *32*, 1604–1617. [CrossRef]

34. Reist, T.A.; Zingg, D.W.; Rakowitz, M.; Potter, G.; Banerjee, S. Multifidelity optimization of hybrid wing-body aircraft with stability and control requirements. *J. Aircr.* **2019**, *56*, 442–456. [CrossRef]

35. Zhang, C.; Zhou, Z.; Zhu, X.P.; Meng, P. Nonlinear static aeroelastic and trim analysis of highly flexible joined-wing aircraft. *AIAA J.* **2018**, *56*, 4988–4999. [CrossRef]

36. Park, J.; Choi, J.Y.; Jo, Y.; Choi, S. Stability and control of tailless aircraft using variable-fidelity aerodynamic analysis. *J. Aircr.* **2017**, *54*, 2148–2164. [CrossRef]

37. Kashiwagura, Y.; Shimoyama, K. A study on the aerodynamic efficiency and static stability of a tailless aircraft. In Proceedings of the 2018 AIAA/ASCE/AHS/ASC Structures, Structural Dynamics, and Materials Conference, Kissimmee, FL, USA, 8–12 January 2018.

38. Peng, C. Relaxed Static Stability Analysis of Flying Wing Aircraft and Research on its Fault-Tolerant Flight Control Methods. Ph.D. Thesis, Navigation, Guidance and Control, Northwestern Polytechnical University, Xi'an, China, 2016. (In Chinese).

39. Phillips, W.F.; Hansen, A.B.; Nelson, W.M. Effects of tail dihedral on static stability. *J. Aircr.* **2006**, *43*, 1829–1837. [CrossRef]

40. Liem, R.P.; Mader, C.A.; Martins, J.R.R.A. Aerostructural design optimization of a 100-passenger regional jet with surrogate-based mission analysis. In Proceedings of the 2013 Aviation Technology, Integration, and Operations Conference, Los Angeles, CA, USA, 12–14 August 2013.

41. Xu, J.; Liu, J.; Zhang, Z.; Wu, X. Spatial–Temporal Transformation for Primary and Secondary Instabilities in Weakly Non-Parallel Shear Flows. *J. Fluid Mech.* **2023**, *959*, A21. [CrossRef]

42. Li, M.; Chen, J.J.; Feng, X.Y.; Qu, F.; Bai, J.Q. An efficient adjoint method for the aero-stealth shape optimization design. *Aerosp. Sci. Technol.* **2021**, *118*, 107017. [CrossRef]

43. Rao, H.; Chen, Y.; Shi, Y.; Yang, T.; Liu, H. Adjoint-Based Aerodynamic Design Optimization and Drag Reduction Analysis of a Military Transport Aircraft Afterbody. *Aerospace* **2023**, *10*, 331. [CrossRef]

44. Shi-Dong, D.; Chen, C.; Nadarajah, S. Adjoint-Based Aerodynamic Optimization of Benchmark CRM Wing. In Proceedings of the 35th AIAA Applied Aerodynamics Conference, Denver, CO, USA, 5–9 June 2017.

45. Masters, D.A.; Poole, D.J.; Taylor, N.J.; Rendall, T.C.S.; Allen, C.B. Impact of Shape Parameterization on Aerodynamic Optimisation of Benchmark Problem. In Proceedings of the 54th AIAA Aerospace Sciences Meeting, San Diego, CA, USA, 4–8 January 2016.

46. Mader, C.A.; Kenway, G.K.W.; Yildirim, A.; Martins, J.R.R.A. ADflow: An Open-Source Computational Fluid Dynamics Solver for Aerodynamic and Multidisciplinary Optimization. *J. Aerosp. Inf. Syst.* **2020**, *17*, 508–527. [CrossRef]

47. Ronzheimer, A. Post-Parameterization of Complex CAD-Based Aircraft- Shapes Using Freeform Deformation Post-Parameterization of Complex CAD-Based Aircraft-Shapes Using Freeform Deformation. In Proceedings of the 8th International Conference on Numerical Grid Generation in Computational Field Simulations, Honolulu, HI, USA, 2–6 June 2002.

48. Samareh, J.A. Aerodynamic Shape Optimization Based on Free-Form Deformation. In Proceedings of the 10th AIAA/ISSMO Multidisciplinary Analysis and Optimization Conference, Albany, NY, USA, 30 August–1 September 2004.

49. Sederberg, T.W.; Parry, S.R. Free-Form Deformation of Solid Geometric Models. *Comput. Graph.* **1986**, *20*, 151–160. [CrossRef]

50. Kenway, G.K.; Kennedy, G.J.; Martins, J.R.R.A. A CAD-free Approach to High-fidelity Aerostructural Optimization. In Proceedings of the 13th AIAA/ISSMO Multidisciplinary Analysis Optimization Conference, Fort Worth, TX, USA, 13–15 September 2010.

51. Luke, E.; Collins, E.; Blades, E. A Fast Mesh Deformation Method Using Explicit Interpolation. *J. Comput. Phys.* **2012**, *231*, 586–601. [CrossRef]

52. Uyttersprot, L. Inverse Distance Weighting Mesh Deformation: A Robust and Efficient Method for Unstructured Meshes. Ph.D. Thesis, Delft University of Technology, Delft, The Netherlands, 2014.

53. Secco, N.R.; Kenway, G.K.W.; He, P.; Mader, C.A.; Martins, J.R.R.A. Efficient Mesh Generation and Deformation for Aerodynamic Shape Optimization. *AIAA J.* **2021**, *59*, 1151–1168. [CrossRef]

54. Du, J.L.; Zong, Y.L.; Bao, H. Shape Adjustment of Cable Mesh Antennas Using Sequential Quadratic Programming. *Aerosp. Sci. Technol.* **2013**, *30*, 26–32. [CrossRef]

55. Fakoor, M.; Zadeh, P.M.; Eskandari, H.M. Developing an Optimal Layout Design of A Satellite System by Considering Natural Frequency and Attitude Control Constraints. *Aerosp. Sci. Technol.* **2017**, *71*, 172–188. [CrossRef]

56. Yang, G.; Ronch, A.D. Aerodynamic Shape Optimisation of Benchmark Problems Using SU2. In Proceedings of the 2018 AIAA/ASCE/AHS/ASC Structures, Structural Dynamics, and Materials Conference, Kissimmee, FL, USA, 8–12 January 2018.

57. Streuber, G.M.; Zingg, D.W. Evaluating the Risk of Local Optima in Aerodynamic Shape Optimization. *AIAA J.* **2021**, *9*, 75–87. [CrossRef]

58. Bobrowski, K.; Ferrer, E.; Valero, E.; Barnewitz, H. Aerodynamic Shape Optimization Using Geometry Surrogates and Adjoint Method. *AIAA J.* **2017**, *55*, 3304–3317. [CrossRef]

59. Wu, N.; Kenway, G.; Mader, C.; Jasa, J.; Martins, J. PyOptSparse: A Python Framework for Large-Scale Constrained Nonlinear Optimization of Sparse Systems. *J. Open Source Softw.* **2020**, *5*, 2564. [CrossRef]

60. Mader, C.A.; Martins, J.R.R.A. Stability-constrained aerodynamic shape optimization of flying wings. *J. Aircr.* **2013**, *50*, 1431–1449. [CrossRef]

61. Wilhelm, K.; Schafranek, D. Landing approach handling qualities of transport aircraft with relaxed static stability. *J. Aircr.* **1986**, *23*, 756–762. [CrossRef]

62. Perez, R.E.; Liu, H.H.T.; Behdinan, K. Multidisciplinary optimization framework for control-configuration integration in aircraft conceptual design. *J. Aircr.* **2006**, *43*, 1937–1948. [CrossRef]

63. Wells, D.P. Cruise Speed Sensitivity Study for Transonic Truss Braced Wing. In Proceedings of the 55th AIAA Aerospace Sciences Meeting, Grapevine, TX, USA, 9–13 January 2017.

64. Bieler, H.; Bier, N.; Bugeda, G.; Periaux, J.; Redondo, D.; Guttila, S.; Pons, J. A common platform for validation of aircraft drag reduction technologies. In Proceedings of the Platform for Aircraft Drag Reduction Innovation, Barcelona, Spain, 29–30 November 2017.

65. Lyu, Z.; Martins, J.R.R.A. Aerodynamic design optimization studies of a blended-wing-body aircraft. *J. Aircr.* **2014**, *51*, 1361–1371. [CrossRef]

66. Reist, T.A.; Zingg, D.W. Aerodynamic Shape Optimization of a Blended-Wing-Body Regional Transport for a Short Range Mission. In Proceedings of the 31st AIAA Applied Aerodynamics Conference, San Diego, CA, USA, 24–27 June 2013.

67. Lyu, Z.; Kenway, G.K.W.; Martins, J.R.R.A. Aerodynamic Shape Optimization Investigations of the Common Research Model Wing Benchmark. *AIAA J.* **2015**, *53*, 968–985. [CrossRef]

68. Ko, A.; Mason, W.; Grossman, B. Transonic aerodynamics of a wing/pylon/strut juncture. In Proceedings of the 21st AIAA Applied Aerodynamics Conference, Orlando, FL, USA, 23-26 June 2003.